




Droplet lift-off from hydrophobic surfaces from impact with soft-hydrogel spheres

Rafsan Rabbi¹ , Akihito Kiyama¹ , John S. Allen² & Tadd Truscott^{1,3} ✉

Droplet impacts on superhydrophobic surfaces may result in complete bouncing, with the absence of contact hysteresis and viscous dissipation leading the droplet to fully rebound off the surface. This rebound usually happens in the retraction phase, when the droplet retracts back after reaching a maximum spread diameter. Here, we present experimental evidence of a bouncing phenomenon where a sessile droplet on a hydrophobic surface bounces off the surface in its spreading phase when a soft deformable hydrogel sphere axisymmetrically impacts the droplet. We term this as ‘Lift-Off’ and propose a simple force balance based on the deformation characteristics of the hydrogel sphere to explain the out-of-plane jump of the droplet during spreading. We observe three different impact regimes, and propose their dependency on a modified elastic ‘Mach’ number (Ma^*) with $Ma^* \approx 0.1$ corresponding to the onset of lift-off. We also report on the unique acoustic signatures of lift-off cases, associated with the capture of air-bubbles through the air-borne retracting droplet rim. These results may have potential applications for drainage and surface cleaning, non-stick surface coating, industrial mixing and plant disease spreading.

¹Utah State University, Mechanical & Aerospace Engineering Department, Logan, UT, USA. ²University of Hawaii at Manoa, Mechanical & Aerospace Engineering Department, Honolulu, HI, USA. ³King Abdullah University of Science & Technology, Physical Science & Engineering Division, Mechanical Engineering Program, Thuwal, Saudi Arabia. ✉email: taddtruscott@gmail.com

Droplet impacts are ubiquitous in nature^{1–6} and have been extensively studied for over a century⁷ because of their immense importance in various industrial and chemical processes^{8–15}. Upon impact, a single droplet expands to reach a maximum diameter, then retracts and rebounds off the surface, with these mechanisms governed through the balance of inertia and capillarity^{16–18}. Droplet impacts on superhydrophobic surfaces have been of particular interest, as these non-wetting impacts may exhibit complete rebound of the impacting droplets due to low viscous dissipation and contact line hysteresis of the surface^{16,17,19–24}. In binary drop impacts, a droplet impacts a sessile droplet on a hydrophobic surface^{25–30} resulting in droplets that may coalesce, and follow the ‘expansion-maximal deformation-retraction-bouncing’ pattern similar to a single droplet impact (Supplementary fig. 1). In this study, we investigate a deviation from this conventional pattern and present a binary impact mechanism where the sessile droplet rebounds off of the superhydrophobic surface in the expansion stage. This is achieved through substituting the incoming droplet in binary impact cases with a soft sphere (hydrogel) as the impactor (Fig. 1). Our experimental observations and theoretical analysis lead to a modified Mach number quantifying three different regimes: the rebound that we term as ‘Lift-off’, the ‘No Lift-off’ and ‘Sheet’ spread of the sessile droplet. Our experiments also show sound producing bubbles formed from an air-borne retracting droplet rim during Lift-off. Hitherto unreported to our knowledge, the observation of an expansion stage lift-off mechanism shows that

the conventional understanding of droplet bouncing is incomplete and deserves further study.

Results and discussion

Figure 1 a shows our experimental setup where a soft deformable hydrogel sphere (diameter $D = 2R$, $99 \pm 0.3\%$ wt. water) impacts a large sessile water droplet with an impact velocity u (uppercase variables represent hydrogel sphere, lowercase represent droplet throughout). The droplet resembles a flattened puddle with height $h_0 \sim 2\kappa^{-1} \sin(\theta_c/2)$, as its maximum azimuthal diameter ($d = 2r$) is greater than the capillary length $\kappa^{-1} \sim \sqrt{\sigma/(\rho g)}$ ³¹ (σ and ρ are the surface tension and density of water, g is acceleration due to gravity). The hydrophobicity of the surface (static contact angle $\theta_c \sim 141^\circ$, Fig. 1a) compels the droplet to take an oval shape on the surface, common for such large puddles ($d > \kappa^{-1}$), with the base contact length l of the droplet always following the $l < d$ rule. Upon impact with the surface, the soft hydrogel sphere significantly deforms, as shown in the image sequence of Fig. 1b. We quantify this deformation using stretch λ and indentation δ ^{32–34} (Fig. 2a, Supplementary fig. 2a). We also take into account the growing base length L (Fig. 1b) of the hydrogel sphere in contact with the surface as it forces the droplet radially outwards from its pinned position.

We call this droplet bouncing mode ‘Lift-Off’, as the droplet is lifted off the surface through the deformation of the impacting soft sphere. One such case is presented in Fig. 1c, where a soft sphere ($D = 16$ mm) impacts a sessile large droplet (volume $V = 0.15$ mL) with impact velocity $u = 1.17$ m/s. In the initial

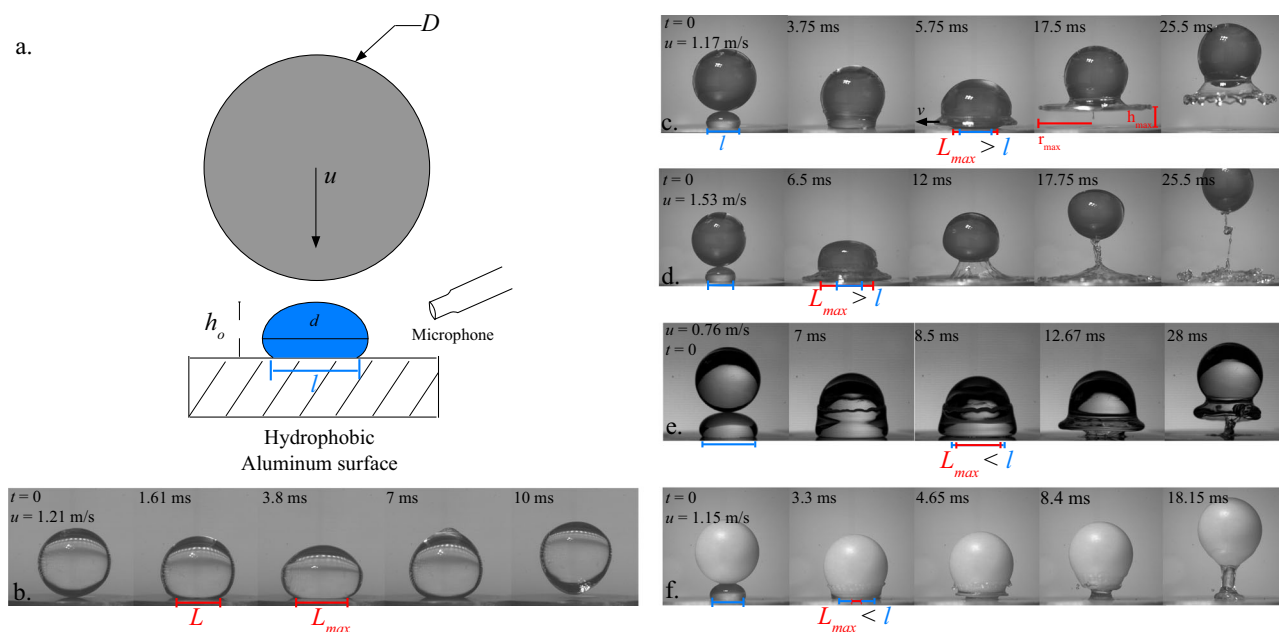


Fig. 1 Experimental setup and sphere-droplet impact dynamics. **a** Schematic of the experiment: a soft hydrogel sphere (diameter D) impacts a droplet resting on a hydrophobic aluminum substrate (contact angle $\theta_c \sim 141^\circ$). The droplet takes on a flattened shape on the surface resembling a large puddle with a maximum height of $h_0 = 2\kappa^{-1} \sin(\theta_c/2)$. The length of the droplet base is l (blue bars, $l < d$ where d is the maximum azimuthal diameter of the droplet). A microphone captures the acoustic signature of the impact event. **b** On impact, the hydrogel sphere ($D = 16$ mm) deforms, with the sphere base length (L , red bars) increasing over time ($t = 0$ –3.8 ms) and reaching a maximum value and then retracting to rebound off the surface. **c** If L surpasses l when the hydrogel sphere impacts a resting droplet, the droplet simultaneously spreads radially ($t = 0$ –5.75 ms) and lifts off vertically during this spreading leaving no water remnant on the surface. h_{max} is measured at r_{max} for consistency, even though the droplet continues to rise higher ($t = 25.5$ ms). **d** Impact velocity of the hydrogel sphere plays an important role in determining whether the droplet would lift-off, as greater impact velocity results in dominant radial spreading and suppression of the droplet rebound. **e** If maximum deformed base length of the hydrogel sphere (L_{max}) is less than l ($t = 8.5$ ms), the droplet fails to completely lift-off on sphere-impact, leaving a water puddle on the surface which connects to the rebounding hydrogel sphere in the form of a water column ($t = 8.5$ –28 ms). **f** This behavior is similar to the impact of a rigid sphere ($D = 16$ mm) on a droplet. Here also, we observe $L_{max} < l$ similar to no lift-off case in (**e**). The droplet does not completely separate from the substrate in this case either, indicating that deformation of the soft sphere is essential to droplet lift-off. Supplementary movies 1–5 show these impact events in their entirety.

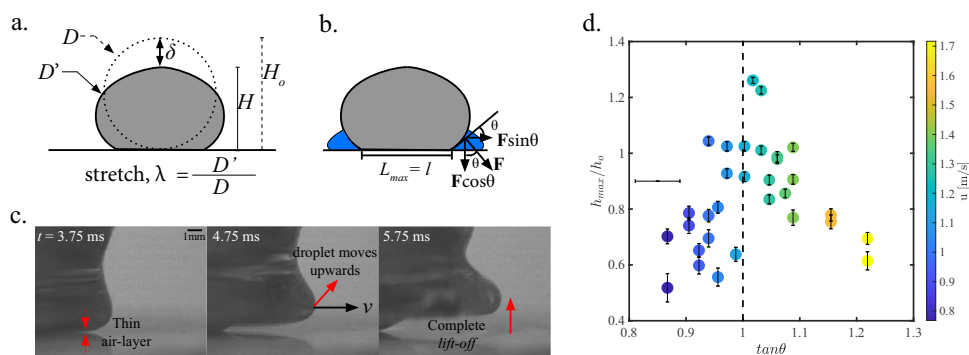


Fig. 2 Hydrogel sphere deformation leads to lift-off of resting droplet. **a** Schematic of the deformation of the impacting soft hydrogel sphere. The initial diameter D increases on impact, leading to sphere height reduction from H_0 . Stretch λ is defined as the ratio of diameter deformation (D'/D , where D' is the instantaneous deformed diameter). The indentation is defined as $\delta = (H_0 - H)$. **b** The deformation of the hydrogel spheres leads to radial base propagation, with the curved sides of the elongating sphere applying a normal force, F , on the droplet. The angle θ represents the curved side of the sphere with the surface (measured when $L_{max} = l$). The vertical and horizontal components of F leads to rebound and radial propagation of the droplet respectively. **c** The two force components affect the droplet in different ways. The horizontal component pushes the droplet rim radially outwards which glides over the thin air layer on the hydrophobic surface (3.75 ms). The vertical force component pushes the rim down, and the rim bounces off the air layer which acts as a spring (4.75 ms). Finally, we see complete lift-off (5.75 ms). Images showing the same drop event shown in Fig. 1a. **d** The angle θ plays an important role in controlling lift-off. The angle θ grows as velocity increases. At lower θ values $F \cos \theta$ dominates, leading to lift-off cases with greater lift-height h_{max} . h_{max} is largest at $\tan \theta \sim 1$. Uncertainty bands are marked with a 95% confidence. Multiple h_{max} values for each θ occur because of varying droplet diameter (d).

moments the water rises up along the sphere surface as it plunges through the droplet. The sphere deforms upon impacting the aluminum substrate and the droplet starts to spread radially along the surface obtaining a maximum spreading velocity of v . The droplet lifts-off entirely from the surface at $t = 5.75$ ms. The droplet hang-time in air is notable ($O(10)$ ms), as the attached droplet moves upward with the rebounding soft sphere, all the while spreading radially to reach a maximum radius r_{max} ($t = 5.75 - 17.5$ ms). This droplet rebound mechanism is significantly different than conventional bouncing^{17,18,21,35} seen in single or drop-on-drop impact cases, where the droplet retracts after reaching r_{max} and then rebounds off the surface. For a sessile droplet with the same amount of water as 1c, if the sphere impact speed u is sufficiently high, we observe suppression of these lift-off characteristics. The droplet rapidly spreads radially along the surface as a thin water sheet in this case (Fig. 1d, $u = 1.53$ m/s), reaching r_{max} before breaking up into multiple droplets due to inertia of the spreading overcoming capillarity. We call these impact cases ‘Sheet’, denoting the formation and expansion of the thin water sheet on the surface after impact. The sheet cases also show a small lift-off of water from the surface at the very initial moments (Fig. 1d, $t = 6.5$ ms), but they are short-lived ($O(1)$ ms) compared to the lift-off cases. Varying the amount of water in the droplet and lowering the sphere impact velocity result in less deformation of the sphere base ($L_{max} < l$). The droplet still spreads radially after sphere impact with a lift-off of the rim, but a liquid column connecting the water attached to the rebounding sphere with a droplet remnant on the surface forms (Fig. 1e), preventing total lift-off. These ‘No Lift-Off’ cases are similar to that of a rigid sphere impacting a sessile droplet. In Fig. 1f a rigid plastic sphere of minimal deformation ($L_{max} \ll l$) lands on a droplet forming a liquid column after rebound, similar to particle impact with shallow pools³⁶. Further, the surface treatments of both sphere and substrate are important for the phenomenon to occur. To demonstrate the effect of each, we performed a few experiments using substrates and spheres with different wettabilities (see Supplementary note 6). Supplementary fig. 6 shows a clean dragon-skin soft sphere with a hydrophilic surface impacting a sessile droplet resulting in lift-off, whereas in Supplementary fig. 7 a rough textured dragon-skin sphere impacting the same sized droplet with the same impact velocity u results in a droplet spread or sheet case (detailed discussion can be found in

Supplementary note 6). Supplementary figs. 8 and 9 show cases where a hydrogel sphere impacts a droplet resting on a hydrophilic surface ($\theta_c = 66^\circ$). Though the impact speed tested ($u \sim 1$ m/s) is fast enough to cause droplet Lift-Off in the hydrophobic cases, the hydrophilic surfaces result in no Lift-Off. These observations suggested that the adhesion between the water droplet and the substrate play a significant role in the overall droplet rebound success. A consistent observation from all these different types of impact is that a large deformation ($L_{max} > l$) enables the sphere to displace the entire droplet contact region, which is essential for complete lift-off.

We propose that this large sphere deformation applies a downward force on the droplet enabling the droplet to lift-off. The deformation characteristics of the soft hydrogel sphere are investigated to validate this hypothesis. The hydrogel spheres used in this study are commercially available cross-linked Acrylamide-chain spheres that experience stretch under impact loading, as defined in Fig. 2a. Compression tests reveal that the hydrogel spheres show a Hertzian response, with the indentation of the sphere $\delta = H_0 - H$ under compression following the slope of $3/2$ (Supplementary fig. 3). This indicates that these soft gel spheres act as elastic materials, and we can use the Hertz theory for deformation of an elastic sphere to determine the Young’s modulus (Supplementary Eq. (3))^{32,34,37}, which in turn can be used to approximate the shear modulus G for the spheres (assuming Poisson’s ratio $\nu = 0.5$ under the incompressibility condition). G has values that range in between 6 kPa and 8 kPa, quantifying the softness of the spheres (see Supplementary note 3 for detailed analysis of G). The characteristics deformation behavior of the hydrogel spheres translates into a growing base length L over time. The resulting continuous change of sphere surface curvature (Fig. 1c) acts as a force F on the droplet as drawn in Fig. 2b. This change in curvature can be tracked by measuring the angle (θ) the sphere surface curvature makes with the substrate (measured when the droplet is not present). θ is measured when $L_{max} = l$ since this displacement condition needs to be fulfilled for droplet lift-off. The force F applied on the droplet by this changing curvature can be broken up into components, with the horizontal component $F \sin \theta$ contributing to the radial spreading of the droplet. The vertical component $F \cos \theta$ acts normal to the impact surface, pushing the droplet downwards. Since the surface is hydrophobic with a Cassie-Baxter

state³⁸, the droplet does not get pinned to the substrate under this normal force. The droplet is instead caught between the sphere and substrate boundaries, and is forced to move up (lift-off) and out (radial spread). The strength of lift-off is $F \cos \theta$, which is a function of impact speed u , but F cannot be easily estimated. Instead the height of lift-off (h_{max}) indicates the strength of this force when normalized by h_0 (Fig. 2d, u from color-bar). Quantitatively, the effect of θ shows that max lift-off occurs when $F \cos \theta = F \sin \theta$. It is evident that lift-off height decreases for higher values of θ , since $F \sin \theta$ far exceeds $F \cos \theta$. These results suggest the possibility of suppression of lift-off at high sphere impact speeds, as confirmed experimentally in Fig. 1e.

Although this force F is difficult to directly quantify, its features provide a physical understanding of the lift-off mechanism in the droplet spreading phase. We can quantify different features of sphere-droplet impacts using elastic deformation, impact kinetic energy and droplet spreading. For a large maximal spreading factor $\lambda_{max} \gg 1$, where $\lambda = D'/D$ with D' being the azimuthal diameter of the impacting sphere during any given moment of deformation, the maximum bulk elastic energy can be expressed as $E_{bulk}^{max} = (\pi D^3/6)G\lambda_{max}^2$ ^{32,33}. Balancing this expression with the impact kinetic energy of the hydrogel sphere $E_k = (1/2)\rho_R(\pi D^3/6)u^2$ (where ρ_R is the hydrogel density), we find

$$\lambda_{max} \sim \frac{u}{\sqrt{G/\rho_R}} \sim \frac{u}{C_s} = Ma \tag{1}$$

where $C_s = \sqrt{G/\rho_R}$ is the shear wave speed in the hydrogel sphere material and Ma is the elastic Mach number for the hydrogel sphere material. Ma characterizes the deformation of the hydrogel sphere. The impact kinetic energy of the sphere translates into radial spreading of the droplet with velocity v . If we use a simplified version of the sphere impact kinetic energy $\rho_R u^2 R^3$ (where $R = D/2$) and the droplet spreading energy $\rho v^2 r^2 h_0$ (where ρ is the density of water, v is the spreading velocity of the droplet (Supplementary fig. 4a), $r = d/2$ and h_0 is the droplet height), we obtain $u \sim \alpha v (r/R)^{3/2} \sqrt{h_0}/r$, where $\alpha = 2.072$ is a fitting parameter. Figure 3a shows the experimentally measured u and v data for different impact combinations of impact velocity ($u = 0.76\text{--}3$ m/s) and different droplet sizes ($V = 0.15\text{--}0.45$ mL), and they are in good agreement with the result of the energy balance. This energy balance is appropriate for low viscosity fluids, where the spreading results from the transfer of a portion of the waterbead kinetic energy into the surface energy of the droplet. Substituting u in Eq. (1) results in the modified Mach number (Ma^*),

$$Ma^* \sim Ma \left(\frac{R}{r}\right)^{3/2} \sqrt{\frac{r}{h_0}}, \tag{2}$$

where $Ma^* = v/C_s$. Ma^* includes all the input parameters involved in the sphere-droplet impact events. Figure 3b plots Ma^* versus L_{max}/l for all impact experiments analyzed, and produces a regime diagram that shows two experimentally observed conditions that need to be satisfied for lift-off. The first is the previously mentioned displacement condition: $L_{max}/l > 1$. The second condition follows from considering that a droplet can move away from the contact surface when the inertial forces overcomes surface tension forces (i.e., Weber number $\geq O(1)$). Here, the droplet can be approximated as a torus (Fig. 2b) with an inner radius of l and a cross section radius of r_{torus} with the velocity of the spreading torus equal to v . Equating the volume of the droplet to the torus yields a reasonable estimate for r_{torus} . We can now calculate Weber number based on the torus as $We_{tor} = \rho v^2 r_{torus} / \sigma$. If we use the velocity of the sheet when the waterbead impact is sufficient to satisfy $L_{max} = l$ we find that $We_{tor} = 1$ satisfies the lift-off condition and corresponds to $v = 0.19\text{--}0.24$ m/s and

$Ma^* = 0.10\text{--}0.12$ for the largest and smallest droplet sizes tested, respectively (Fig. 3a, b).

The Ma^* value can determine the transition from lift-off to sheets as well but the value is dependent on the volume of the droplet. For instance, for the smallest droplet ($V = 0.15$ ml) and a Weber number based on the sheet thickness ($We_{sh} = \rho v^2 h / \sigma$) should transition to sheets when $We_{sh} \gg 1$. The thickness (h) is estimated by conserving the volume from the original droplet to a disk with an outer radius $r(v)$ and an inner radius $L(u)$. Applying these assumptions for $We_{sh} \sim 10$ the sheet velocity is then 2.05 m/s or $Ma^* = 1.02$ for the transition of the 0.15 ml droplet and 1.45 m/s or $Ma^* = 0.73$ for the transition of the 0.30 ml droplet. The coupling of u , C_s and v is important here because the behavior of the water is dependent on all three and thus, explains the broad transition band.

Stiffer spheres tend to skip over the lift-off regime and go from no lift-off to sheets. In cases where C_s is large, the impact velocity (u) required for $L_{max}/l > 1$ is also large, resulting in a large v . Thus, a stiffer sphere will be in the no lift-off regime at low u and then jump to the sheet regime at high u skipping the lift-off regime unless l is very small. This explains why the sphere in Fig. 1f does not lift-off despite the same impact velocity of Fig. 1c.

Using Eq. (2), we can also make a prediction about the time it takes for the droplet to lift-off from the surface after hydrogel sphere impact. The time to lift-off or τ_c is analogous to contact time of conventional single droplet rebound, which in the latter case is proportional to $\sqrt{\rho r^3 / \sigma}$, an increasing function of droplet radius r that does not depend on droplet impact velocity^{29,35}. Herein, lift-off happens earlier in the droplet spreading phase, and is approximated to be $\tau_c \sim r/u$. Rearranging Eq. (2),

$$\tau_c \sim \frac{r}{u} \sim \frac{R^{3/2}}{v \sqrt{h_0}}, \tag{3}$$

a detailed derivation given in the Supplementary note 4. Experimental measurements follow the proposed scaling as shown in Fig. 3c.

We can also estimate the maximum spreading ratio (r_{max}/r) of a droplet after the soft sphere impact. For single or drop-on-drop conventional bouncing cases in low viscosity fluids, the spreading ratio is a function of droplet Weber number, $r_{max}/r \sim We^{1/4}$ where $We = \rho u^2 r / \sigma$ ^{16,29}. We can arrive at this expression by applying volume conservation to the droplet spreading after impact. In hydrogel sphere-droplet impact cases, the transfer of kinetic energy from sphere to droplet drives spreading. The initial volume of the droplet can be scaled as $r^2 h$, where the droplet thickness h can be obtained through $\sqrt{\sigma / (\rho g)}$. After the sphere impacts the droplet, the droplet undergoes deformation, with r and h changing over time. Clanet, et al.¹⁶ proposed that for a single droplet impact, the typical acceleration experienced by the spreading droplet scales as u^2/r , where u is the droplet impact speed. This would alter the formulation for the droplet thickness to $h = \sqrt{\sigma / (\rho u^2)}$. Following the same argument, and using the droplet spreading velocity v in place of u , we can scale the droplet maximum spread as $(r_{max}^2 - R^2) \sqrt{\sigma / (\rho v^2)}$. We subtract sphere radius R from the droplet maximum radius, since after impact the droplet takes on a torus shape around the sphere. Subsequently, we obtain the spreading ratio,

$$\frac{r_{max}}{r} \sim \left[\left(\frac{R}{r}\right)^2 + We_v^{1/2} \left(\frac{h_0}{r}\right) \right]^{1/2} \tag{4}$$

where $We_v = \rho v^2 r / \sigma$ is the droplet spreading Weber number. Detail derivation for Eq. (4) is given in the Supplementary note 5. Figure 3d shows a comparison of the experimentally

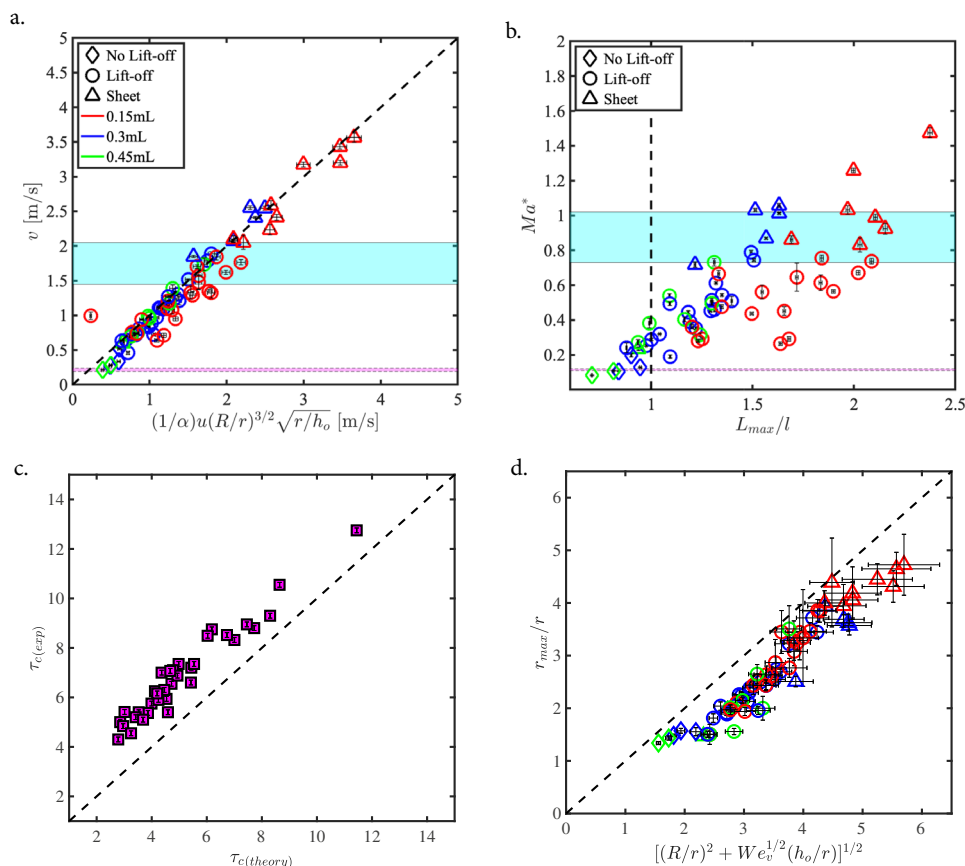


Fig. 3 Energy balance and regime diagram. **a** Energy balance between the sphere impact and droplet spreading reveals maximum droplet spreading velocity v to be a function of impact velocity u , and sphere and droplet sizes respectively. Plotting the experimentally measured v against the calculated functional form shows a one to one relation, using a fitting parameter of $\alpha = 2.072$. **b** This leads to the formulation of a modified Mach number Ma^* , which plotted against L_{max}/l shows the range $0.10 < Ma^* < 0.12$ to be the tentative onset of lift-off (magenta band). This regime plot also confirms the earlier stated condition of lift-off, $L_{max}/l > 1$. The cyan band at $0.73 < Ma^* < 1.02$ reveals the Ma^* range where we would expect to see separation between the lift-off and sheet regime. The experimental data largely follows this prediction band, with most of the sheet cases happening at $Ma^* > 0.73$. **c** The lift-off time (τ_c) of the droplet, measured from the moment of sphere impact on droplet to the first moment of droplet rim leaving the surface, plotted as a function of Ma^* . The experimentally measured values of τ_c scales with the lift-off times found from Eq. (3). **d** The spreading ratio of the droplet after soft sphere impact can be predicted using the scaling law proposed through Eq. (4). The experimentally measured spreading factor values exhibit the same predicted slope. In all the plots, the red, blue, and green marker colors denote the droplet volume, $V = 0.15, 0.3$ and 0.45 mL respectively. Uncertainty bands are marked with a 95% confidence.

measured spreading factor data to values predicted through Eq. (4). The comparison reveals the proposed relationship works well over a range of different droplet volumes. This only holds for liquid droplets of low viscosity whereas higher viscosity has been shown to inhibit the spreading of droplet after sphere impact¹⁶.

Figure 4 a presents an image sequence of the retraction dynamics of a lifted-off droplet in flight after it has reached maximum spreading ratio r_{max}/r . At this point, the droplet spreading velocity $v \sim 0$, and the capillarity of water dominates, causing the droplet rim to move inwards ($t = 14\text{--}26$ ms). As the droplet remains attached to the upwards moving rebounding sphere, the thin water sheet that connects the rim of the droplet with the sphere also moves upward. These two motions create a hollow liquid column over time, with the inbound droplet rim at the bottom. The surface tension in the rim forms multiple fingers which later collapse inward ($t = 26\text{--}33$ ms) leading to the hollow column closing from below, trapping a few air bubbles ($t = 33\text{--}38$ ms). These bubbles coalesce and form a large bubble which oscillates with a distinctive frequency ($t = 41$ ms, Fig. 4b). We capture the sound of bubble entrapment and oscillations using a synchronized microphone (Earthworks QTC-40,

bandwidth 5 Hz–40 KHz) sampling at 96 KHz. The acoustic signal reveals a clear peak and high-frequency oscillation around 41 ms, indicating that this lift-off bouncing mode has distinct acoustic characteristics (Fig. 4c,d). The spectrum shows the resonance frequency of the bubble to be $f_s \sim 4$ KHz. Using the Minnaert frequency formula for air bubbles³⁹, we calculate the approximate volume equivalent bubble radius R_V to be 0.85 mm which is close to the measured bubble volume equivalent radius of 1.1 mm from the image (Fig. 4b). This further strengthens the argument that lift-off has unique acoustic characteristics. It is to be noted here that this signature acoustic behavior of lift-off cases are generally dominant at the low impact velocity lift-off cases. As impact velocity increases, the lift-off cases transition to the sheet cases, where instead of having one dominant bubble oscillation multiple oscillations and noise throughout the impact event follow from the capillary breaking of the sheet into multiple droplets (see Supplementary fig. 5).

In summary, we have presented experimental observations along with the theoretical analysis of a new type of droplet rebound mechanism in binary impact cases for a deformable hydrogel sphere impacting a sessile droplet on a hydrophobic surface. This lift-off of water droplet results from the deforming

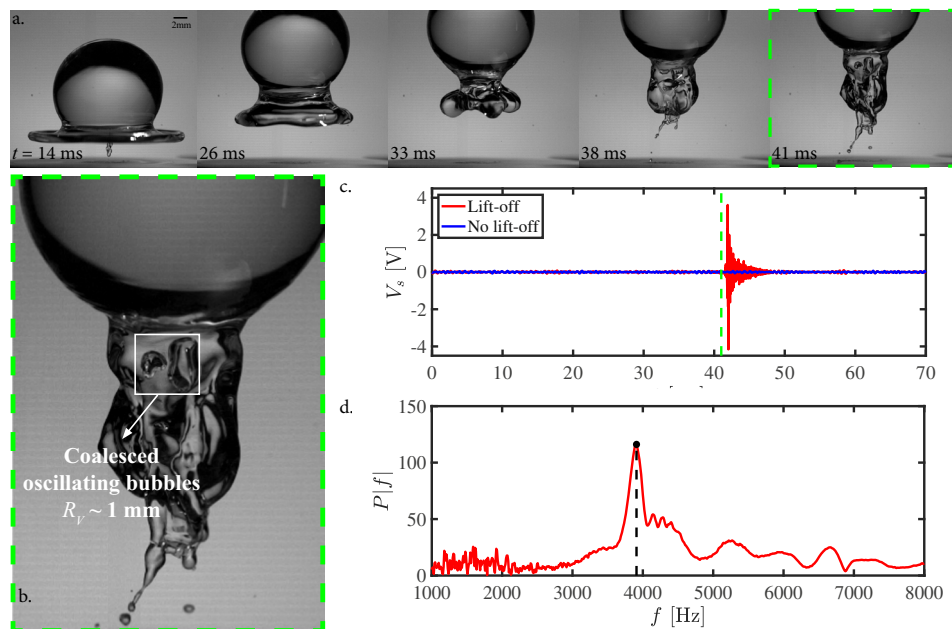


Fig. 4 Bubble capture and collapse in mid-air through droplet retraction in lift-off cases. **a** Image sequence showing the retraction phase of the droplet. The hydrogel sphere impacts a droplet (volume, $V = 0.30$ mL) at time $t = 0$ with an impacting velocity of 1.17 m/s. The droplet bounces off and reaches the maximum spreading radius at $t = 14$ ms. Afterwards, the rim starts to retract inwards with the upwards motion of the rebounding sphere, a reverse cone develops with several spherical fingers at the edge of the rim ($t = 26$ ms– 33 ms). This hollow cone collapses on itself ($t = 38$ ms) trapping a significant amount of air inside the resultant liquid jet ($t = 38$ – 41 ms). **b** The air inside coalesces into a large bubble (white box) of radius R_v , that oscillates at resonance frequency. **c** The oscillation is captured in the microphone as an acoustic signal. Acoustic signal captured for a no lift-off case is also plotted for comparison. As the no lift-off case show no bubble capture (Fig. 1f), no discernible sounds are measured. 0 ms marks the time of sphere impact. **d** A power spectrum indicates a resonance frequency $f_s \sim 4$ kHz.

characteristics of the soft hydrogel sphere. This type of impact can also produce two more regimes: ‘No Lift-Off’ and ‘Sheet’. We propose a modified Ma^* number to quantify different regimes, and propose two conditions for lift-off: (i) $L_{max}l > 1$ and (ii) $0.1 < Ma^* < 0.12$. In addition to these fundamental observations, our findings show bubble entrapment through an air-borne retracting droplet rim. The uses for hydrogel spheres are growing for chemical and microfluidics processes^{40,41}, such that this water-scooping technique along with air bubble entrapment and acoustic signature in the receding phase may be useful in certain scenarios, e.g., mixing and emulsification, surface cleaning. It may also have potential implications in plant disease spreading through droplet bouncing⁶ with increasing use of hydrogel spheres as crop protection agents⁴².

Methods

Preparation of hydrogel spheres and hydrophobic surface. The soft hydrogel spheres used for this study are commercially available growing spheres from the reseller *Educational Innovations* (GB-710). The dehydrated hydrogel particles were submerged in 100% de-ionized water, and were left to grow undisturbed for 24 h. The mean final mass of the spheres used for the impact experiments was 2.5285 ± 0.2386 g. An aluminum plain surface was used as the metal substrate, made hydrophobic by applying Glaco-Mirror Coat Zero superhydrophobic coating, which yielded a static contact angle of $\theta_c \sim 141^\circ$. A polystyrene sphere (also from *Educational Innovations*) of diameter $D = 16$ mm, mass = 2.10 g and shear modulus $G = 750$ MPa (data cited from manufacturer’s manual) was used for the solid sphere impact experiments.

Binary drop experiments. The hydrogel spheres were dropped from different heights, ranging from 30 mm to 400 mm. The free falling spheres impact the droplets and then the aluminum substrate below with velocities in 0.75 m/s– 3 m/s range. Data from 71 individual drop tests are presented, covering 22 different drop heights ranging from 30 mm to 350 mm (see Supplementary Table 1). The droplets were deposited on the surface using a pipette, with the volume of water in the droplet carefully controlled. Two droplet volumes were used for most cases, 0.15 ± 0.05 mL and 0.30 ± 0.05 mL, and for a few cases a 0.45 ± 0.05 mL droplets were also used. Surface tension of the droplets was 72.8 mN/m. A Phantom v2511

high-speed camera was used to record the impact events at 31,000 frames per second, with an LED array worked as the backlight. Images from the video were processed in MATLAB.

Data availability

The data generated and analyzed during the current study, the codes to reproduce the data plots, and links to the Supplementary information sets are available at the KAUST Library public repository (<http://hdl.handle.net/10754/671206>). The raw image data will be made available upon request.

Received: 30 August 2021; Accepted: 12 December 2022;

Published online: 22 December 2022

References

- Danielli, J. F., Pankhurst, K., Riddiford, A. & Salzberg, H. Surface phenomena in chemistry and biology. *J. Electrochem. Soc.* **106**, 226C (1959).
- Joung, Y. S. & Buie, C. R. Aerosol generation by raindrop impact on soil. *Nat. Commun.* **6**, 1–9 (2015).
- Ekern, P. C. Raindrop impact as the force initiating soil erosion. *Soil Sci. Soc. Am. J.* **15**, 7–10 (1951).
- Ensikat, H. J., Ditsche-Kuru, P., Neinhuis, C. & Barthlott, W. Superhydrophobicity in perfection: the outstanding properties of the lotus leaf. *Beilstein J. Nanotechnol.* **2**, 152–161 (2011).
- Watson, G. S., Gellender, M. & Watson, J. A. Self-propulsion of dew drops on lotus leaves: a potential mechanism for self cleaning. *Biofouling* **30**, 427–434 (2014).
- Nath, S. et al. ‘sneezing’ plants: Pathogen transport via jumping-droplet condensation. *J. R. Soc. Interfac.* **16**, 20190243 (2019).
- Worthington, A. M. *A study of splashes* (Longmans, Green, and Company, 1908).
- Liu, Z. & Kim, A. K. A review of water mist fire suppression systems—fundamental studies. *J. Fire Prot. Eng.* **10**, 32–50 (1999).
- Mawhinney, J. R. & Back, G. G. Water mist fire suppression systems. In *SFPE Handbook of fire protection engineering*, 1587–1645 (Springer, 2016).

10. Abramzon, B. & Sirignano, W. Droplet vaporization model for spray combustion calculations. *Int. J. Heat. Mass Transf.* **32**, 1605–1618 (1989).
11. Chandra, S. & Avedisian, C. On the collision of a droplet with a solid surface. *Proc. R. Soc. Lond. Ser. A: Math. Phys. Sci.* **432**, 13–41 (1991).
12. Dhiman, R., McDonald, A. G. & Chandra, S. Predicting splat morphology in a thermal spray process. *Surf. Coat. Technol.* **201**, 7789–7801 (2007).
13. Aziz, S. D. & Chandra, S. Impact, recoil and splashing of molten metal droplets. *Int. J. Heat. Mass Transf.* **43**, 2841–2857 (2000).
14. Wijshoff, H. The dynamics of the piezo inkjet printhead operation. *Phys. Rep.* **491**, 77–177 (2010).
15. Stringer, J. & Derby, B. Limits to feature size and resolution in ink jet printing. *J. Eur. Ceram. Soc.* **29**, 913–918 (2009).
16. Clanet, C., Béguin, C., Richard, D. & Quéré, D. Maximal deformation of an impacting drop. *J. Fluid Mech.* **517**, 199 (2004).
17. Bird, J. C., Dhiman, R., Kwon, H.-M. & Varanasi, K. K. Reducing the contact time of a bouncing drop. *Nature* **503**, 385–388 (2013).
18. Bartolo, D., Josserand, C. & Bonn, D. Retraction dynamics of aqueous drops upon impact on nonwetting surfaces. *arXiv preprint physics/0509133* (2005).
19. Rein, M. Phenomena of liquid drop impact on solid and liquid surfaces. *Fluid Dyn. Res.* **12**, 61–93 (1993).
20. Rioboo, R., Tropea, C. & Marengo, M. Outcomes from a drop impact on solid surfaces. *Atomization Sprays* **11**, 155–165 (2001).
21. Richard, D. & Quéré, D. Bouncing water drops. *EPL (Europhys. Lett.)* **50**, 769 (2000).
22. Richard, D., Clanet, C. & Quéré, D. Contact time of a bouncing drop. *Nature* **417**, 811–811 (2002).
23. Yarin, A. L. Drop impact dynamics: splashing, spreading, receding, bouncing. *Annu. Rev. Fluid Mech.* **38**, 159–192 (2006).
24. Liu, Y. et al. Pancake bouncing on superhydrophobic surfaces. *Nat. Phys.* **10**, 515–519 (2014).
25. Boreyko, J. B. & Chen, C.-H. Self-propelled dropwise condensate on superhydrophobic surfaces. *Phys. Rev. Lett.* **103**, 184501 (2009).
26. Graham, P. J., Farhangi, M. M. & Dolatabadi, A. Dynamics of droplet coalescence in response to increasing hydrophobicity. *Phys. Fluids* **24**, 112105 (2012).
27. Castrejón-Pita, J., Kubiak, K., Castrejón-Pita, A., Wilson, M. & Hutchings, I. Mixing and internal dynamics of droplets impacting and coalescing on a solid surface. *Phys. Rev. E* **88**, 023023 (2013).
28. Wang, Y. & Bourouiba, L. Non-isolated drop impact on surfaces. *J. Fluid Mech.* **835**, 24 (2018).
29. Damak, M. & Varanasi, K. Expansion and retraction dynamics in drop-on-drop impacts on nonwetting surfaces. *Phys. Rev. Fluids* **3**, 093602 (2018).
30. Ramírez-Soto, O., Sanjay, V., Lohse, D., Pham, J. T. & Vollmer, D. Lifting a sessile oil drop from a superamphiphobic surface with an impacting one. *Sci. Adv.* **6**, eaba4330 (2020).
31. De Gennes, P.-G., Brochard-Wyart, F. & Quéré, D. *Capillarity and wetting phenomena: drops, bubbles, pearls, waves* (Springer Science & Business Media, 2013).
32. Tanaka, Y., Yamazaki, Y. & Okumura, K. Bouncing gel balls: impact of soft gels onto rigid surface. *EPL (Europhys. Lett.)* **63**, 146 (2003).
33. Arora, S. et al. Impact of beads and drops on a repellent solid surface: a unified description. *Phys. Rev. Lett.* **120**, 148003 (2018).
34. Ye, X. & van der Meer, D. Hydrogel sphere impact cratering, spreading and bouncing on granular media. *arXiv preprint arXiv:2104.00243* (2021).
35. Okumura, K., Chevy, F., Richard, D., Quéré, D. & Clanet, C. Water spring: a model for bouncing drops. *EPL (Europhys. Lett.)* **62**, 237 (2003).
36. Hauk, T., Bonaccorso, E., Villedieu, P. & Trontin, P. Theoretical and experimental investigation of the melting process of ice particles. *J. Thermophys. Heat. Transf.* **30**, 946–954 (2016).
37. Matsuda, Y., Fukui, S., Kamiya, R., Yamaguchi, H. & Niimi, T. Impact cratering on a granular bed by hydrogel spheres having intermediate property between solid and liquid. *Phys. Rev. E* **99**, 032906 (2019).
38. Quéré, D. Non-sticking drops. *Rep. Prog. Phys.* **68**, 2495 (2005).
39. Minnaert, M. Xvi. on musical air-bubbles and the sounds of running water. *Lond. Edinb. Dublin Philos. Mag. J. Sci.* **16**, 235–248 (1933).
40. Cabodi, M. et al. A microfluidic biomaterial. *J. Am. Chem. Soc.* **127**, 13788–13789 (2005).
41. Beebe, D. J. et al. Functional hydrogel structures for autonomous flow control inside microfluidic channels. *Nature* **404**, 588–590 (2000).
42. Peteu, S. F., Oancea, F., Siciua, O. A., Constantinescu, F. & Dinu, S. Responsive polymers for crop protection. *Polymers* **2**, 229–251 (2010).

Acknowledgements

The authors would like to thank Dr. Silvana Martini of the USU food science department for her gracious permission to let the authors use the AR G2 rheometer in her laboratory for the rheology measurement. The authors would also like to thank Dr. Randy Hurd from Weber State University, Utah, US and Dr. Zhao Pan from University of Waterloo, Canada for valuable inputs and discussions. J.A. acknowledges partial support from University of Hawaii at Manoa and the ONR Redhill project #N00014-20-1-2651. The authors would also like to thank Dr. Sandip Dighe from King Abdullah University of Science & Technology, Thuwal, KSA for the Supplementary experiments.

Author contributions

J.A. and T.T. designed the research, R.R., J.A., A.K., and T.T. performed experiments, R.R., A.K., and T.T. conceived the scaling laws and theory, R.R. analyzed the data, R.R. wrote the paper, R.R., J.A., A.K., and T.T. edited, and J.A. and T.T. provided financial support.

Competing interests

The authors declare no competing interests.

Additional information


Supplementary information The online version contains supplementary material available at <https://doi.org/10.1038/s42005-022-01114-8>.

Correspondence and requests for materials should be addressed to Tadd Truscott.

Peer review information *Communications Physics* thanks Jonathan Pham and the other, anonymous, reviewer(s) for their contribution to the peer review of this work. This article has been peer reviewed as part of Springer Nature's [Guided Open Access](#) initiative.

Reprints and permission information is available at <http://www.nature.com/reprints>

Publisher's note Springer Nature remains neutral with regard to jurisdictional claims in published maps and institutional affiliations.

 **Open Access** This article is licensed under a Creative Commons Attribution 4.0 International License, which permits use, sharing, adaptation, distribution and reproduction in any medium or format, as long as you give appropriate credit to the original author(s) and the source, provide a link to the Creative Commons license, and indicate if changes were made. The images or other third party material in this article are included in the article's Creative Commons license, unless indicated otherwise in a credit line to the material. If material is not included in the article's Creative Commons license and your intended use is not permitted by statutory regulation or exceeds the permitted use, you will need to obtain permission directly from the copyright holder. To view a copy of this license, visit <http://creativecommons.org/licenses/by/4.0/>.

© The Author(s) 2022